



Design and synthesis of three-dimensional hybrid Ruddlesden-Popper nickelate single crystals

Feiyu Li ¹, Ning Guo,² Qiang Zheng,² Yang Shen,³ Shilei Wang,¹ Qihui Cui,¹ Chao Liu,¹ Shanpeng Wang,¹ Xutang Tao,^{1,*} Guang-Ming Zhang,^{4,5,†} and Junjie Zhang ^{1,‡}

¹State Key Laboratory of Crystal Materials and Institute of Crystal Materials, Jinan, Shandong 250100, China

²CAS Key Laboratory of Standardization and Measurement for Nanotechnology, CAS Center for Excellence in Nanoscience, National Center for Nanoscience and Technology, Beijing 100190, China

³Key Laboratory of Artificial Structures and Quantum Control, School of Physics and Astronomy, Shanghai Jiao Tong University, Shanghai 200240, China

⁴State Key Laboratory of Low-Dimensional Quantum Physics, Department of Physics, Tsinghua University, Beijing 100084, China

⁵Frontier Science Center for Quantum Information, Beijing 100084, China



(Received 21 February 2024; accepted 12 April 2024; published 8 May 2024)

The advancement of technologies relies on the discovery of new materials with emerging physical properties that are determined by their crystal structures. Ruddlesden-Popper (R-P) phases with a formula of $A_{n+1}B_nX_{3n+1}$ ($n = 1, 2, 3, \dots, \infty$) are among one of the most widely studied classes of materials due to their electrical, optical, magnetic, and thermal properties as well as their combined multifunctional properties. In R-P phases, intergrowth is well known in the short range; however, no existing compounds have been reported to have different n mixed in bulk single crystals. Here we design a hybrid R-P nickelate $\text{La}_2\text{NiO}_4 \cdot \text{La}_3\text{Ni}_2\text{O}_7$ by alternatively stacking bilayers, which is the active structural motif in the high- T_c superconductor $\text{La}_3\text{Ni}_2\text{O}_7$ and single layers of the antiferromagnetic insulator La_2NiO_4 . We report the successful synthesis of $\text{La}_2\text{NiO}_4 \cdot \text{La}_3\text{Ni}_2\text{O}_7$ single crystals, and x-ray diffraction and real-space imaging via scanning transmission electron microscopy (STEM) show that the crystal structure consists of single layers and bilayers of NiO_6 octahedral stacking alternatively perpendicular to the ab plane, characterized by the orthorhombic $Immm$ (No. 71) space group. Resistivity measurements indicate a metallic ground state and a peculiar resistivity maximum around 140 K. Density functional theory (DFT+ U) calculations corroborate this finding and reveal that both the bilayer and the single layer are metallic and that the single layer becomes paramagnetic metallic due to the charge transfer via LaO layers. The discovery of $\text{La}_2\text{NiO}_4 \cdot \text{La}_3\text{Ni}_2\text{O}_7$ opens a door to access a family of three-dimensional hybrid R-P phases with the formula of $A_{n+1}B_nX_{3n+1} \cdot A'_{m+1}B'_mX'_{3m+1}$ ($n \neq m$), which potentially host a plethora of emerging physical properties for various applications.

DOI: [10.1103/PhysRevMaterials.8.053401](https://doi.org/10.1103/PhysRevMaterials.8.053401)

I. INTRODUCTION

Quasi-two-dimensional layered Ruddlesden-Popper (R-P) oxide perovskites display various emerging physical properties ranging from high-temperature superconductivity [1,2], colossal magnetoresistance [3], metal-insulator transition [4], and multiferroicity [5,6]. The ternary oxide system La-Ni-O contains a homologous series of layered phases of general composition $(\text{LaO})(\text{LaNiO}_3)_n$, in which n layers of perovskite-type LaNiO_3 are separated by single NaCl-type LaO layers [7]. The average oxidation state of Ni in $\text{La}_{n+1}\text{Ni}_n\text{O}_{3n+1}$ ($n = 1, 2, 3, \dots, \infty$) varies from 2+ for $n = 1$ to 2.5+ for $n = 2$ and to 3+ for $n = \infty$. The first member of this series, La_2NiO_4 , is known to have an orthorhombic structure with the rotated NiO_6 octahedrons, being an antiferromagnetic Mott insulator at low temperatures [8]. Recently, the signature of superconductivity with $T_c \sim 80$ K above

14 GPa has been reported in the second member of this series, the bilayer nickelate $\text{La}_3\text{Ni}_2\text{O}_7$ [9–12]. At ambient pressure, it crystallizes in the orthorhombic $Amam$ space group with a Ni-O-Ni angle of 168° , and it undergoes a structural transition to $Fmmm$ with a Ni-O-Ni angle of 180° under high pressure [9]. So, there is a natural question whether there exist other high- T_c superconducting nickelates at ambient pressure, which share the similar crystal structure of $\text{La}_3\text{Ni}_2\text{O}_7$ under high pressure. Besides high- T_c superconductors, are there any other types of nickelates in which rich physical properties emerge in the electronic phase diagram?

In this paper, we design a family of perovskites by stacking n - and m -layer perovskites in long-range order, yielding three-dimensional $A_{n+1}B_nO_{3n+1} \cdot A'_{m+1}B'_mO_{3m+1}$ hybrid oxide perovskites. As an example, we successfully synthesize single crystals of $\text{La}_2\text{NiO}_4 \cdot \text{La}_3\text{Ni}_2\text{O}_7$ ($n = 1, m = 2$). The key structural motif for the electronic properties in $\text{La}_3\text{Ni}_2\text{O}_7$ is the bilayer Ni-O planes. On average, each $\text{Ni}^{2.5+}$ has fully occupied bonding orbitals and empty antibonding orbitals of d_{z^2} [9]. Incorporation of the bilayer NiO_2 into a new compound is expected to maintain the key electronic features of $\text{La}_3\text{Ni}_2\text{O}_7$. In La_2NiO_4 , the single-layer NiO_2 planes

*jingti535tao@163.com

†gmzhang@mail.tsinghua.edu.cn

‡junjie@sdu.edu.cn

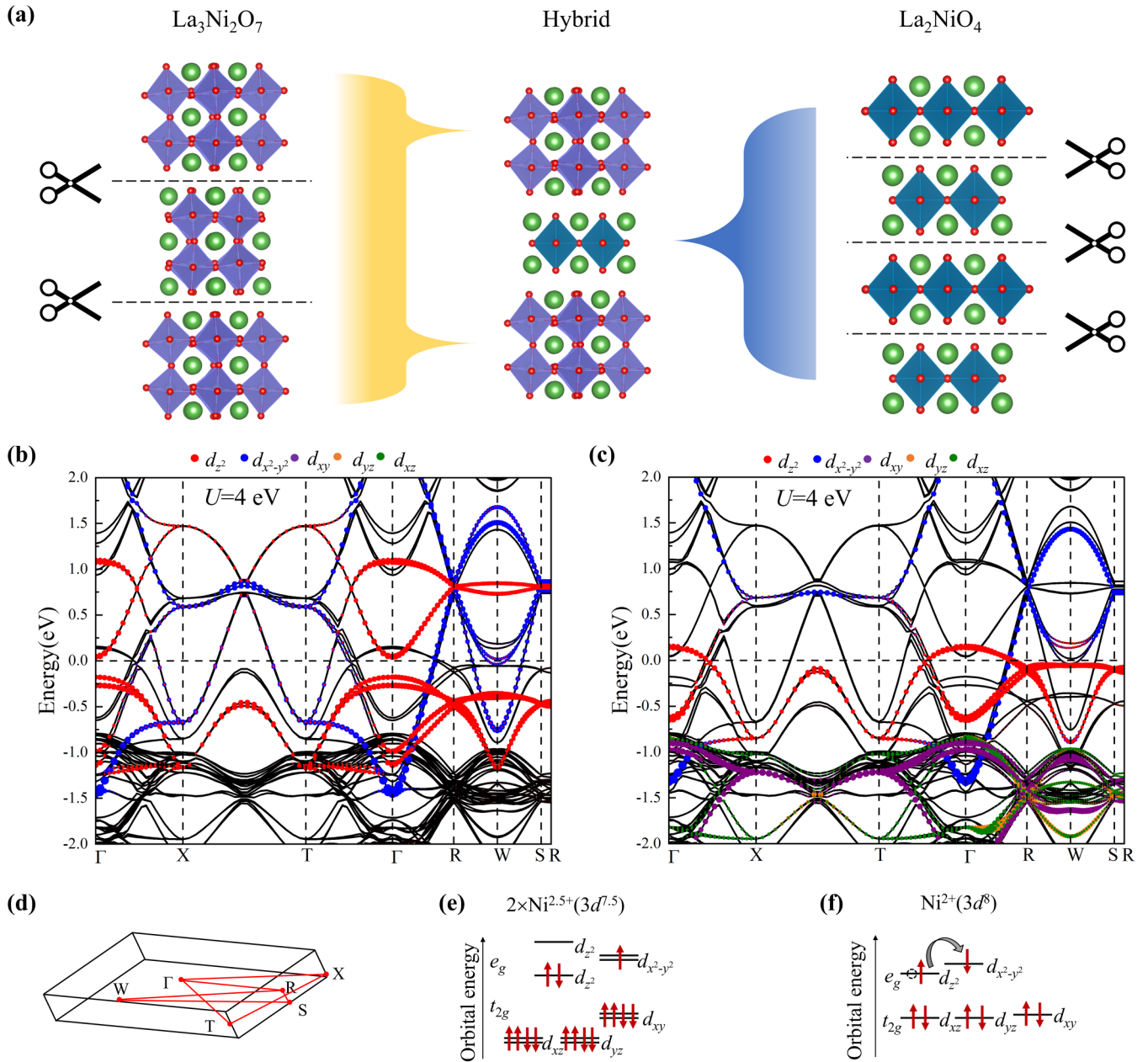


FIG. 1. Materials design strategy for hybrid $\text{La}_2\text{NiO}_4 \cdot \text{La}_3\text{Ni}_2\text{O}_7$ and calculated electronic structure. (a) Illustration of our design strategy to hybridize bilayer, the structural motif that is responsible for high-temperature superconductivity in $\text{La}_3\text{Ni}_2\text{O}_7$, and single layer in the three-dimensional (3D) antiferromagnetic La_2NiO_4 in the long-range order. (b) Orbital projected weights of the bilayer NiO_2 in the hybrid $\text{La}_2\text{NiO}_4 \cdot \text{La}_3\text{Ni}_2\text{O}_7$ crystal given by the density functional theory. (c) Orbital projected weights of the single NiO_2 in the hybrid $\text{La}_2\text{NiO}_4 \cdot \text{La}_3\text{Ni}_2\text{O}_7$ crystal given by the density functional theory. (d) Schematic of the 3D body-centered orthorhombic Brillouin zone. The red lines correspond to the paths of the electronic bands in (b) and (c). (e) Energy levels of the unit with two $\text{Ni}^{2.5+}$ ($3d^{7.5}$) in the bilayer under the crystal field. The d_{z^2} orbitals of two Ni cations in the neighboring layers form the bonding and antibonding states. (f) Energy levels of the unit with Ni^{2+} ($3d^8$) in the single layer under the crystal field. The dotted circle indicates a hole generated by charge transfer from d_{z^2} to $d_{x^2-y^2}$ orbitals.

form a two-dimensional spin-1 Heisenberg antiferromagnetic insulator on a square lattice with a Néel temperature of ~ 330 K [8]. Hole doping in La_2NiO_4 results in a rich electronic phase diagram, consisting of an antiferromagnetic insulator, charge and spin stripes, checkboard charge order, and pseudogap phenomena [13]. Figure 1(a) presents our materials design strategy to hybridize bilayer from $\text{La}_3\text{Ni}_2\text{O}_7$ and

single layer from La_2NiO_4 in the long-range order perpendicular to the Ni-O plane. By tailoring La_2NiO_4 into single layers, the antiferromagnetic long-range order is expected to be destroyed and only spin fluctuations are left. The combination of a magnetic single layer and superconducting bilayers is predicted to host emerging properties that belong to neither La_2NiO_4 nor $\text{La}_3\text{Ni}_2\text{O}_7$.

II. RESULTS AND DISCUSSION

With the given design, we use a flux method to synthesize the single crystals of $\text{La}_2\text{NiO}_4 \cdot \text{La}_3\text{Ni}_2\text{O}_7$ at ambient pressure. Conventionally, single crystals of rare-earth nickelates with higher nickel valence are prepared either by high oxygen pressure floating-zone techniques or a high-pressure flux method [7,14]. Recent advancements in growing single crystals of trilayer $\text{La}_4\text{Ni}_3\text{O}_{10}$ have been achieved without high pressure, i.e., single crystals can be prepared at ambient pressure using K_2CO_3 as a flux [15]. By changing the initial molar ratio of La and Ni to 5:3, single crystals of $\text{La}_2\text{NiO}_4 \cdot \text{La}_3\text{Ni}_2\text{O}_7$ with dimensions up to 120 μm in length and 80 μm in thickness were successfully prepared. Figure 2(a) presents the scanning electron microscopy (SEM) image of a typical single crystal with sizes of $110 \times 80 \times 50 \mu\text{m}^3$ (more crystals are shown in Fig. S1 in the Supplemental Material [16]). The regular shape with a smooth and clean surface of the sample indicates high quality of the as-grown single crystal. Energy dispersive spectrometer (EDS) measurements on single crystals result in La:Ni of 1.77 (sample 1) and 1.70 (sample 2), consistent with the expected 5:3 for $\text{La}_2\text{NiO}_4 \cdot \text{La}_3\text{Ni}_2\text{O}_7$.

The crystal structure at room temperature was determined using in-house x-ray single-crystal diffraction. The initial unit cell determination resulted in a unit cell with $c \sim 16.5 \text{ \AA}$, which lies in the middle of La_2NiO_4 with $c \sim 12.7 \text{ \AA}$ [17] and $\text{La}_3\text{Ni}_2\text{O}_7$ with $c \sim 20.5 \text{ \AA}$ [9]. This observation strongly suggests that it is a long-range intergrowth of single-layer and bilayer NiO_2 planes. Subsequent analysis (see Fig. S2 in the Supplemental Material [16]) leads to an orthorhombic body-centered unit cell with lattice parameters of $a = 5.4296(2) \text{ \AA}$, $b = 5.4330(2) \text{ \AA}$, and $c = 33.2067(12) \text{ \AA}$. Figures 2(b) and 2(c) display selected high-symmetry reciprocal lattice planes ($hk0$) and ($h0l$) reconstructed from a total of 2728 frames. The observed peaks obey the selection rule of $h + k + l = \text{even}$, consistent with the body-centered unit cell. The structure was solved using the *Immm* (No. 71) space group, and the refinements converged to $R_1 = 6.05\%$ and $wR_2 = 10.23\%$. Figure S3 in the Supplemental Material [16] shows the observed structural factor F as a function of the calculated values. Ideally the calculated F equals to the observed F as indicated by the red line. Details of crystal parameters, data collection, and structure refinement are summarized in Table S1 in the Supplemental Material [16].

Figure 2(d) presents the crystal structure of $\text{La}_2\text{NiO}_4 \cdot \text{La}_3\text{Ni}_2\text{O}_7$ using the ball-and-stick model. The unit cell contains two bilayers and two single layers. The asymmetric unit consists of six La atoms, three Ni atoms, and eight O atoms. The La atoms are surrounded by 9 or 13 oxygen atoms with bond length in the range of 2.28(5)–2.778(11) \AA . The Ni atoms are bonded to six oxygen atoms with bond lengths of 1.916(10)–2.227(18) \AA for the bilayer [Fig. 2(e)] and 1.920 26(5)–2.34(5) \AA for the single layer [Fig. 2(f)]. The Ni-O bond distance along the c axis for the bilayer is 3%–6.5% longer than that of $\text{La}_3\text{Ni}_2\text{O}_7$ or $\text{La}_2\text{PrNi}_2\text{O}_7$ measured at 14–15 GPa [9,18]. The out-of-plane Ni-O-Ni angle within the bilayer is 180° [Fig. 2(e)], the same as that of $\text{La}_3\text{Ni}_2\text{O}_7$ in the superconducting state under high pressure [9]. These crystallographic data suggest that $\text{La}_2\text{NiO}_4 \cdot \text{La}_3\text{Ni}_2\text{O}_7$ is a potential material for exploring high-temperature superconductivity.

Rietveld refinement on powder diffraction data using the single-crystal model was carried out to verify our structural model [Fig. 2(g)]. The refinement converged to the following figures of merit: $R_{\text{expt}} = 3.02\%$, $R_{\text{wp}} = 5.79\%$, and Goodness of fit (GOF) = 1.92 with lattice parameters of $a = 5.41730(9) \text{ \AA}$, $b = 5.45820(9) \text{ \AA}$, and $c = 33.1844(6) \text{ \AA}$. These reasonable parameters and the small difference between the calculated and the observed intensity strongly support the crystal structure from single-crystal diffraction. We found that there exists a small amount of $\text{La}_3\text{Ni}_2\text{O}_7$ (6.7 wt %) impurity (not shown in the figure) with the remaining 93.3 wt % attributable to $\text{La}_2\text{NiO}_4 \cdot \text{La}_3\text{Ni}_2\text{O}_7$. The powders were prepared by pulverizing crystals that previously did not pass through 300-mesh sieves (crystals > 50 μm on edge). There exist two possibilities for the source of the impurity: (1) single crystals of $\text{La}_3\text{Ni}_2\text{O}_7$ and (2) inclusions or intergrowth of $\text{La}_3\text{Ni}_2\text{O}_7$ on $\text{La}_2\text{NiO}_4 \cdot \text{La}_3\text{Ni}_2\text{O}_7$. We performed single-crystal x-ray diffraction experiments multiple times to select $\text{La}_2\text{NiO}_4 \cdot \text{La}_3\text{Ni}_2\text{O}_7$ single crystals, and we occasionally picked up $\text{La}_3\text{Ni}_2\text{O}_7$ single crystals. By further considering the clean single-crystal diffraction pattern and scanning transmission microscopy (STEM) results (shown below), the first source is likely the case. It is difficult to distinguish $\text{La}_2\text{NiO}_4 \cdot \text{La}_3\text{Ni}_2\text{O}_7$ from $\text{La}_3\text{Ni}_2\text{O}_7$ single crystals using a microscope due to their similar morphology.

To further verify the long-range intergrowth of single-layer and bilayer NiO_2 planes, real-space imaging via STEM was performed. A typical HAADF-STEM (high-angle annular dark field-STEM) image in the [110] projection shown in Fig. 3(a) and a lower-magnification HAADF image shown in Fig. S4 in the Supplemental Material [16] indicate perfectly ordered stacking of the alternating bilayers and single layers in the length scale of tens of nanometers in the $\text{La}_2\text{NiO}_4 \cdot \text{La}_3\text{Ni}_2\text{O}_7$ single crystals. Such a long-range ordered stacking can be revealed by chemical distributions of La and Ni from EDS maps in Fig. 3(b). As shown in Figs. S5 and S6 in the Supplemental Material [16], the HAADF-STEM imaging was also performed along the [100] zone axis, further confirming the fully ordering sequences of the alternating bilayers and single layers.

Figure 3(c) shows the magnetic susceptibility of the as-grown $\text{La}_2\text{NiO}_4 \cdot \text{La}_3\text{Ni}_2\text{O}_7$ single crystals in the temperature range of 25–350 K under an external magnetic field of 0.4 T. Between 25 and ~ 200 K, it exhibits the Curie-Weiss behavior, indicating the presence of weakly interacting local magnetic moments. Above ~ 200 K, the magnetic susceptibility is almost temperature independent, consistent with Pauli paramagnetism. The data (not shown) between 2 and 25 K does not show any magnetic long-range order but is sample dependent. Figure 3(d) displays the resistivity of a polycrystalline pellet of $\text{La}_2\text{NiO}_4 \cdot \text{La}_3\text{Ni}_2\text{O}_7$ pulverized from single crystals and sintered at 900° C in air. In addition to the expected metal-insulator transition at high temperatures above 350 K, a peculiar resistivity maximum occurs around 140 K on warming, in sharp contrast to the other R-P nickelates such as the insulating behavior of La_2NiO_4 at low temperatures [8], the metal-to-metal transition in bilayer $\text{La}_3\text{Ni}_2\text{O}_7$ and trilayer $\text{La}_4\text{Ni}_3\text{O}_{10}$ [19–21], and the metal-to-insulator transition in RNiO_3 ($R = \text{Pr} - \text{Lu}, \text{Y}$) [22]. The underlying physics of this resistivity maximum may be related to the presence of charge

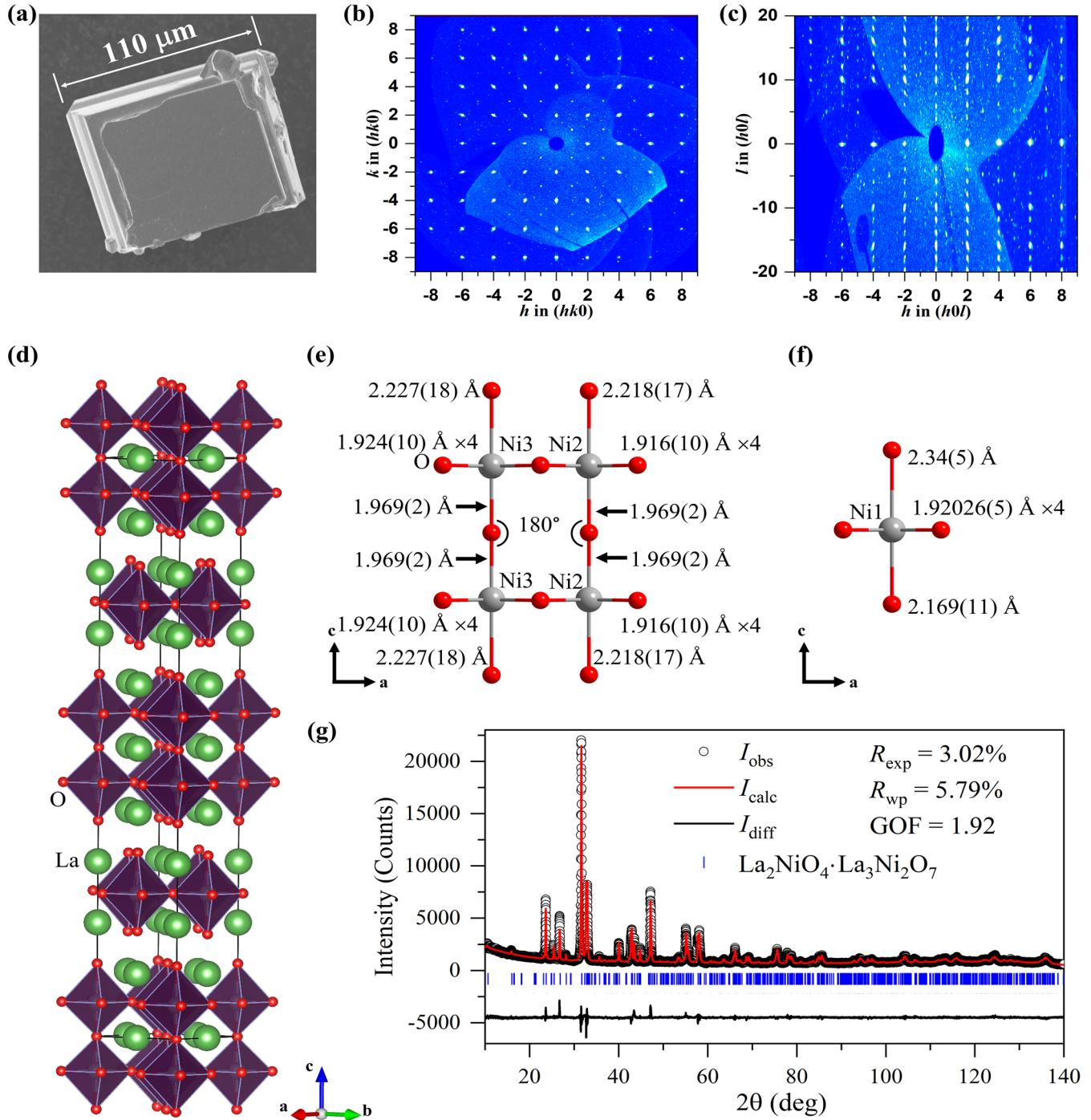


FIG. 2. Crystal structure of the single-layer and bilayer hybridized nickelate $\text{La}_2\text{NiO}_4 \cdot \text{La}_3\text{Ni}_2\text{O}_7$. (a) A SEM image of an as-grown single crystal with dimensions of $110 \times 80 \times 50 \mu\text{m}^3$. (b) Reconstructed $(hk0)$ planes from in-house x-ray single-crystal diffraction data collected at 296(2) K. (c) Reconstructed $(h0l)$ planes from in-house x-ray single-crystal diffraction data collected at 296(2) K. (d) Structural model obtained from x-ray single-crystal diffraction. (e) Ball-and-stick drawings of the NiO_6 octahedrons with bond distances and bond angles in the bilayer NiO_2 . (f) Ball-and-stick drawing of the NiO_6 octahedrons with bond distances in the single-layer NiO_2 . (g) Rietveld refinement on powder diffraction data collected on pulverized single crystals obtained from flux growth. Structural model in (d) was used as a starting model.

transfer between the insulating single layer and metallic bilayers in this hybrid structure.

With the determined structure of single crystals and low-temperature physical properties, we performed the numerical calculation of density functional theory (DFT+ U) for the single-crystal $\text{La}_2\text{NiO}_4 \cdot \text{La}_3\text{Ni}_2\text{O}_7$ within a nonmagnetic

solution. With an intermediate on-site Coulomb interaction $U = 4$ eV, we find that the electronic states near the Fermi level are dominated by the Ni $3d_{x^2-y^2}$ and $3d_z^2$ orbitals in the energy window of -2 to 2 eV, while the Ni t_{2g} orbital electrons are far below the Fermi energy (see Fig. S7 in the Supplemental Material [16]). The Ni $3d_z^2$ orbitals are mixed

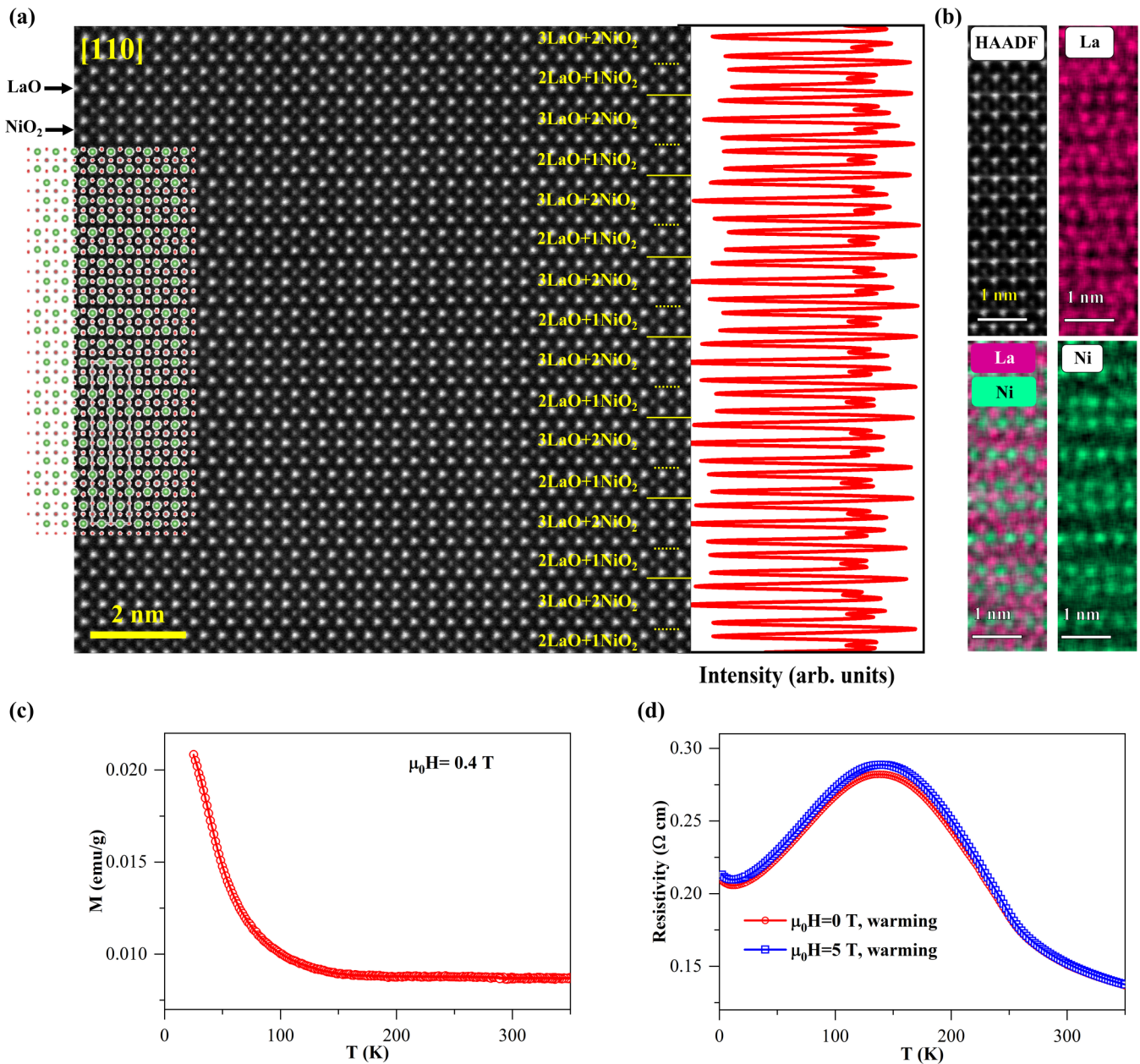


FIG. 3. Real-space imaging of the structure and physical properties of $\text{La}_2\text{NiO}_4 \cdot \text{La}_3\text{Ni}_2\text{O}_7$. (a) A typical atomic-scale HAADF-STEM image in the projection of [110] with overlaid crystal structure model; the right panel is the line intensity profile for rows of all atomic columns. (b) EDS maps for La and Ni and mixed color map of them. (c) Magnetic susceptibility of as-grown single crystals. (d) Resistivity on warming under an external magnetic field of 0 and 5 T. Note, a single crystal is too small to put four leads on; polycrystalline pellets were used and treated at 900°C in air prior to making contacts.

with oxygen $2p_z$ orbitals across the Fermi level, indicating strong covalent hybridization among these orbitals (see Fig. S7 in the Supplemental Material [16]). The rare-earth element La has little hybridization with Ni and O $2p_z$ orbitals (see Fig. S8 in the Supplemental Material [16]). Actually, it is better to present complementary plots of the Ni e_g bands disentangled according to their origin from Ni sites in the different structural units. Figure 1(b) displays the orbital projected weights of the structural units with NiO_6 octahedral bilayers in the hybrid $\text{La}_2\text{NiO}_4 \cdot \text{La}_3\text{Ni}_2\text{O}_7$ crystal, where the $3d_z^2$ orbitals form the σ -bonding and antibonding bands via the interlayer apical oxygens, opening a small energy gap at

the Fermi energy [Fig. 1(d)]. This gives rise to fully occupied bonding orbitals and empty antibonding orbitals of d_z^2 , very similar to the electronic structure of $\text{La}_3\text{Ni}_2\text{O}_7$ [9]. However, the orbital projected weights of the structural units with NiO_6 octahedral single layers in the hybrid $\text{La}_2\text{NiO}_4 \cdot \text{La}_3\text{Ni}_2\text{O}_7$ crystal show that the $3d_{x^2-y^2}$ electrons are nearly free with parabolic dispersions along the Γ - R direction, the $3d_z^2$ orbital band is hole doped with a narrow bandwidth, and the Van Hove singularity of correlated $3d_z^2$ electrons along the R - S direction may induce a possible electronic instability [Fig. 1(c)]. These numerical results can be simplified as shown in Figs. 1(e) and 1(f) and are consistent with the paramagnetic

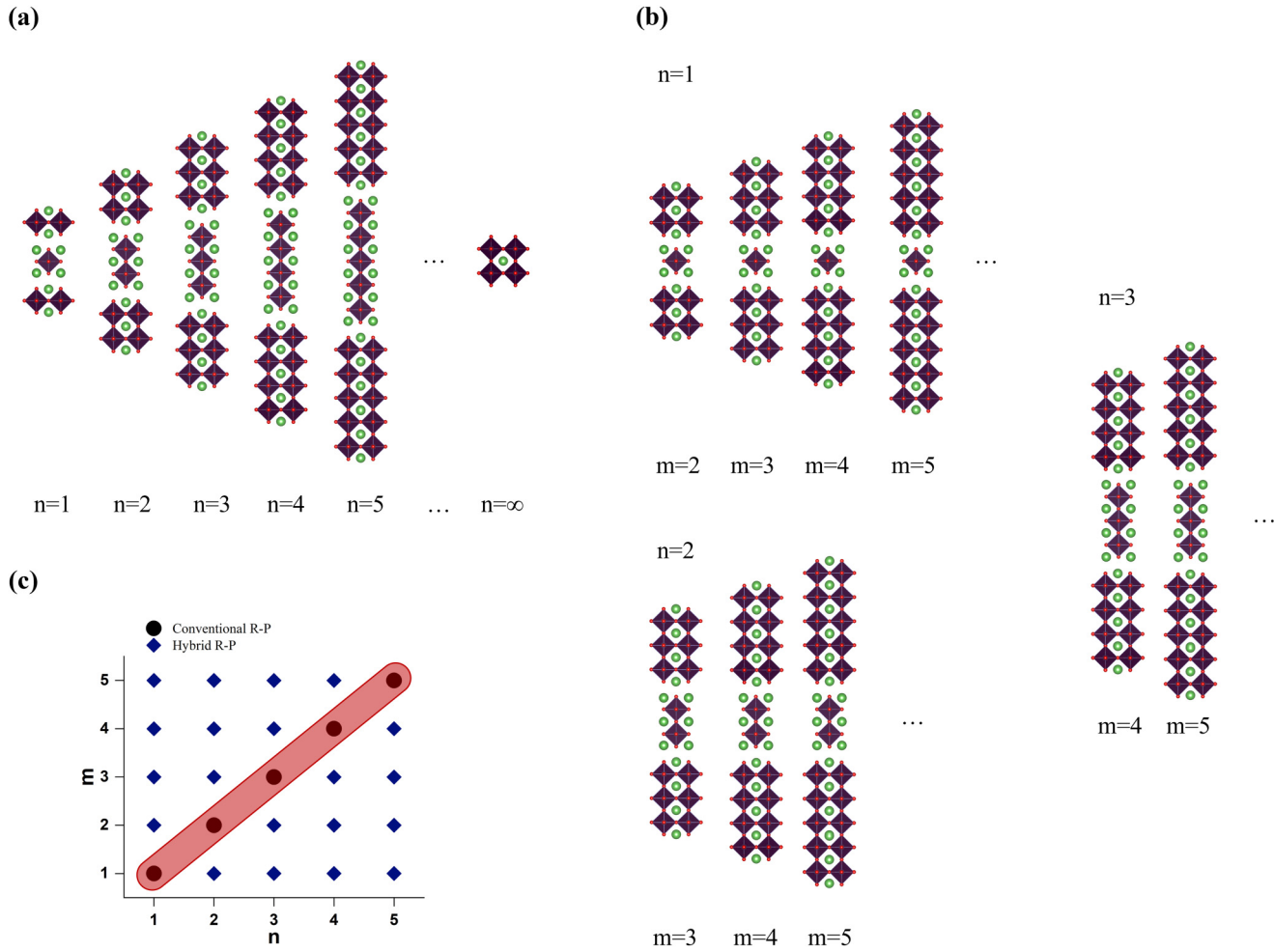


FIG. 4. Hybrid Ruddlesden-Popper (R-P) phases as a class of quantum materials that potentially host emerging physical properties. (a) Conventional R-P nickelates with the formula of $\text{La}_{n+1}\text{Ni}_n\text{O}_{3n+1}$ ($n = 1, 2, 3, \dots$). Note n are integers and only one n exists in a single compound. (b) Hybrid R-P nickelate family with the formula of $\text{La}_{n+1}\text{Ni}_n\text{O}_{3n+1} \cdot \text{La}_{m+1}\text{Ni}_m\text{O}_{3m+1}$ ($m, n = 1, 2, 3, \dots$ and $m \neq n$). $\text{La}_2\text{NiO}_4 \cdot \text{La}_3\text{Ni}_2\text{O}_7$ is one member of this family with $n = 1$ and $m = 2$. (c) General R-P phases with the formula of $A_{n+1}B_nX_{3n+1} \cdot A'_{m+1}B'_mX'_{3m+1}$ ($m, n = 1, 2, 3, \dots$). In these compounds, A and A' are usually alkaline-earth- or rare-earth-metal ions (e.g., Ca, Sr, Ba, La-Lu) or organic groups [e.g., CH_3NH_3 , $\text{CH}(\text{NH}_2)_2$]; B and B' are transition metal ions (e.g., Ti, V, Mn, Fe, Co, Ni, Nb, Zr, Ru, Sn, Pb); X and X' are anions (e.g., O, Cl, Br, I).

metallic behavior observed in the low-temperature experimental result.

Therefore, our proposed long-range hybrid single-layer and bilayer NiO_2 planes in a single compound have been realized in $\text{La}_2\text{NiO}_4 \cdot \text{La}_3\text{Ni}_2\text{O}_7$, as evidenced by x-ray single-crystal diffraction, Rietveld refinement on powder diffraction, and real-space imaging of the structure using STEM. In fact, this compound just represents one member of a family of long-range hybrid R-P nickelates. Figure 4(a) shows the conventional R-P nickelates with the formula of $\text{La}_{n+1}\text{Ni}_n\text{O}_{3n+1}$ ($n = 1, 2, 3, \dots, \infty$) [23]. By expanding this R-P nickelate via introducing different building blocks, the hybrid R-P family of nickelates $\text{La}_{n+1}\text{Ni}_n\text{O}_{3n+1} \cdot \text{La}_{m+1}\text{Ni}_m\text{O}_{3m+1}$ ($m, n = 1, 2, 3, \dots$, and $m > n$) can be formed as shown in Fig. 4(b). Among them, $\text{La}_2\text{NiO}_4 \cdot \text{La}_3\text{Ni}_2\text{O}_7$ is the first member of this family with $n = 1$ and $m = 2$. By tuning conditions of materials synthesis during flux growth [15] or high-pressure floating-zone growth [20], it is expected that $\text{La}_2\text{NiO}_4 \cdot$

$\text{La}_4\text{Ni}_3\text{O}_{10}$ ($n = 1, m = 3$), $\text{La}_2\text{NiO}_4 \cdot \text{La}_5\text{Ni}_4\text{O}_{13}$ ($n = 1, m = 4$), $\text{La}_2\text{NiO}_4 \cdot \text{La}_6\text{Ni}_5\text{O}_{16}$ ($n = 1, m = 5$), $\text{La}_3\text{Ni}_2\text{O}_7 \cdot \text{La}_4\text{Ni}_3\text{O}_{10}$ ($n = 2, m = 3$), $\text{La}_3\text{Ni}_2\text{O}_7 \cdot \text{La}_5\text{Ni}_4\text{O}_{13}$ ($n = 2, m = 4$), $\text{La}_3\text{Ni}_2\text{O}_7 \cdot \text{La}_6\text{Ni}_5\text{O}_{16}$ ($n = 2, m = 5$), $\text{La}_4\text{Ni}_3\text{O}_{10} \cdot \text{La}_5\text{Ni}_4\text{O}_{13}$ ($n = 3, m = 4$), $\text{La}_4\text{Ni}_3\text{O}_{10} \cdot \text{La}_6\text{Ni}_5\text{O}_{16}$ ($n = 3, m = 5$), and $\text{La}_5\text{Ni}_4\text{O}_{13} \cdot \text{La}_6\text{Ni}_5\text{O}_{16}$ ($n = 4, m = 5$), ... can be synthesized.

Even more nickelates can be designed and explored if one mixes different rare-earth ions. Synthesis of these bulk samples may be challenging for $n, m > 3$. As an alternative way, the preparation of thin films using techniques like molecular-beam epitaxy [24,25] potentially have a better chance. Figure 4(c) shows the general R-P phases $A_{n+1}B_nX_{3n+1} \cdot A'_{m+1}B'_mX'_{3m+1}$, where A and A' are usually alkaline-earth- or rare-earth-metal ion (e.g., Ca, Sr, Ba, La-Lu) or organic groups [e.g., CH_3NH_3 , $\text{CH}(\text{NH}_2)_2$], B and B' are transition metal ions (e.g., Ti, V, Mn, Fe, Co, Ni, Nb, Zr, Ru, Sn, Pb), and X and X' are anions (e.g., O, Cl, Br, I) and $m, n = 1, 2, 3, \dots, \infty$. With the success of $\text{La}_2\text{NiO}_4 \cdot \text{La}_3\text{Ni}_2\text{O}_7$ in

the nickelate system, it is straightforward to explore more general hybrid R-P phases in other transition metal oxides including cobaltites for spin transition [26], manganites for colossal magnetoresistance [3], halide perovskites for photovoltaic applications [27], and x-ray or γ -ray detection [28,29]. Indeed, a superlattice of $\text{Sr}_2\text{IrO}_4 \cdot \text{Sr}_3\text{Ir}_2\text{O}_7$ with dimensions of a few microns in thickness, thicker than layer-by-layer grown thin films but thinner than typical bulk crystals, have been achieved [30], and synthesis of bulk single crystals of this material and characterization of its physical properties are intriguing.

Furthermore, in the trilayer or bilayer R-P nickelates, the apical oxygen atoms between NiO_2 layers can be removed upon topotactical reduction [31,32], but the in-plane oxygen atoms remain unchanged, making $\text{La}_2\text{NiO}_4 \cdot \text{La}_3\text{Ni}_2\text{O}_6$ or $\text{La}_2\text{NiO}_4 \cdot \text{La}_4\text{Ni}_3\text{O}_8$ a unique system to explore R-P and the Ni-O planar (T' -structure) hybrid phase. For other members of the hybrid R-P nickelates ($n > 1, m > n$), if successful, it will be interesting to perform topotactical reduction to hybrid T' -structure nickelates for rich emergent physical properties such as charge order and high- T_c superconductivity [33].

III. CONCLUSION

In summary, by tailoring the bilayer NiO_2 from the recently discovered high- T_c superconductor $\text{La}_3\text{Ni}_2\text{O}_7$ and the single layer from the antiferromagnetic insulator La_2NiO_4 , we have designed a long-range hybrid R-P nickelate $\text{La}_2\text{NiO}_4 \cdot \text{La}_3\text{Ni}_2\text{O}_7$. The realization of such a structure in real materials has been achieved via flux growth at ambient pressure. The crystal structure of $\text{La}_2\text{NiO}_4 \cdot \text{La}_3\text{Ni}_2\text{O}_7$ consists of single layers and bilayers stacking alternatively perpendicular to the ab plane as determined from single-crystal x-ray diffraction. The structure is corroborated by Rietveld refinement on powder diffraction and confirmed by real-space imaging using STEM. This material shows the Curie-Weiss behavior as indicated by magnetic susceptibility and a resistivity maximum at low temperatures. The discovery of $\text{La}_2\text{NiO}_4 \cdot \text{La}_3\text{Ni}_2\text{O}_7$ opens up horizons to a family of hybrid R-P phases with the formula of $A_{n+1}B_nX_{3n+1} \cdot A'_{m+1}B'_mX'_{3m+1}$ ($n \neq m$), which potentially host a plethora of emerging physical properties including high-temperature superconductivity, colossal magnetoresistance, metal-insulator transition, multiferroicity, and optoelectronic properties.

Note added. Recently, an independent work by Chen *et al.* from Argonne National Laboratory reported the synthesis and resistivity measurement of $\text{La}_2\text{NiO}_4 \cdot \text{La}_4\text{Ni}_3\text{O}_{10}$ ($n = 1, m = 3$) single crystals [34]. The existence of $\text{La}_2\text{NiO}_4 \cdot \text{La}_4\text{Ni}_3\text{O}_{10}$ is also independently reported by Pupal *et al.* from Max-Planck-Institute for Solid State Research [35] and Wang *et al.* from Michigan State University [36]. This so-called “1313” compound just serves as the second example of our proposed hybrid R-P family of nickelates.

ACKNOWLEDGMENTS

Work at Shandong University was supported by the National Natural Science Foundation of China (Grants No. 12074219 and No. 12374457), the 111 Project 2.0

(BP2018013), the TaiShan Scholars Project of Shandong Province (tsqn201909031), the QiLu Young Scholars Program of Shandong University, the Crystalline Materials and Industrialization Joint Innovation Laboratory of Shandong University and Shandong Institutes of Industrial Technology (Z1250020003), and the Project for Scientific Research Innovation Team of Young Scholars in Colleges and Universities of Shandong Province (2021KJ093). G.M.Z. acknowledges the support of National Key Research and Development Program of China (Grant No. 2023YFA1406400). J.Z. and F.L. thank Professor Jian Zhang for his help with in-house single-crystal x-ray diffraction. J.Z. thanks Dr. Yu-Sheng Chen and Dr. Teyan Chang from The University of Chicago for stimulating discussions.

APPENDIX: SOME DETAILS OF EXPERIMENTS AND NUMERICAL CALCULATIONS

1. Single-crystal growth

Single crystals of $\text{La}_2\text{NiO}_4 \cdot \text{La}_3\text{Ni}_2\text{O}_7$ were grown using a flux method with K_2CO_3 as a flux at ambient pressure. A mixture of preheated La_2O_3 (Sigma-Aldrich, 99.99%), Ni (Alfa Aesar, 99.8%, particle size 5 – 15 μm), and anhydrous K_2CO_3 (Aladdin, 99.99%) in the molar ratio of 5:6:210 was loaded in an Al_2O_3 crucible with a lid in order to minimize the evaporation. The procedure for crystal growth is similar to that of $\text{La}_4\text{Ni}_3\text{O}_{10}$ [15].

2. X-ray diffraction

Single-crystal x-ray diffraction data were collected using a Bruker AXS D8 Venture (Mo $K\alpha_1$ radiation, $\lambda = 0.71073 \text{ \AA}$) diffractometer at room temperature. A single crystal with dimensions of $40 \times 57 \times 58 \mu\text{m}^3$ was used to determine the structure of $\text{La}_2\text{NiO}_4 \cdot \text{La}_3\text{Ni}_2\text{O}_7$. For data collection, Ω and Φ scans were used, and 2728 frames were collected. Indexing was performed using Bruker APEX4 software [37]. Data integration and cell refinement were performed using SAINT, and multiscan absorption corrections were applied using the SADABS program [37]. Using OLEX2 [38], the structure was solved with the XT structure solution program using intrinsic phasing and refined with the XL refinement package using least squares minimization [37]. All La and Ni atoms (except O atoms) were modeled using anisotropic displacement parameters, and the refinements converged for $I > 2\sigma(I)$, where I is the intensity of reflections and $\sigma(I)$ is standard deviation. Further details of the crystal structure investigations may be obtained from the joint CCDC/FIZ Karlsruhe online deposition service by quoting the deposition number CSD 2313044. Powder x-ray diffraction data were collected on a Bruker AXS D2 Phaser diffractometer at room temperature using Cu $K\alpha$ radiation ($\lambda = 1.5418 \text{ \AA}$) in the 2θ range of $10^\circ - 140^\circ$ with a scan step size of 0.01° and a scan time of 2.1 s per step. TOPAS 6 was used for Rietveld refinement where the single-crystal structural model was used as a starting model. Refinement parameters include background (Chebyshev function, order 5), sample displacement, lattice parameters, crystallite size L , and strain G .

3. SEM

The morphology of the as-grown crystals was examined using a scanning electron microscope. The scanning electron microscope images were obtained by a Hitachi S-4800 microscope incident electron of 5.0 kV.

4. EDS

The x-ray spectrometer EDAX GENESIS XM2 system 60 \times on S-4800 was used for qualitative and quantitative analysis of the as-grown crystals. The experiments were carried out on three single crystals.

5. STEM

STEM specimens were prepared by crushing $\text{La}_2\text{NiO}_4 \cdot \text{La}_3\text{Ni}_2\text{O}_7$ single crystals in ethanol. A drop of the suspensions was deposited on lacey carbon-coated copper grids and dried in air. HAADF-STEM images were acquired at an accelerating voltage of 300 kV on a double-aberration-corrected transmission electron microscope (Spectra 300, Thermo Fisher Scientific), equipped with a field-emission electron source. The probe convergence semiangle and inner collection semiangle are 25.0 and 49 mrad, respectively. EDS data were obtained with a Super-X EDS detector.

6. Resistivity

The resistivity of $\text{La}_2\text{NiO}_4 \cdot \text{La}_3\text{Ni}_2\text{O}_7$ was measured using the standard four-probe method on polycrystalline pellets under an external magnetic field of 0 and 5 T. Note, a single crystal is too small to put four leads on; polycrystalline pellets were used and treated at 900 $^\circ$ C in air prior to making contacts with silver paste. A Quantum Design physical property

measurement system (PPMS; DynaCool-9) was used to measure resistivity in the temperature range of 2–300 K at a warming rate of 3.0 K/min.

7. Magnetic susceptibility

DC magnetization of as-grown $\text{La}_2\text{NiO}_4 \cdot \text{La}_3\text{Ni}_2\text{O}_7$ single crystals was measured using a PPMS DynaCool 9 T. ZFC-W (Zero-field cooling with data collected on warming), FC-C (field cooling and data collected on cooling), and FC-W (field cooling and data collected on warming) data were collected between 2 and 300 K under an external magnetic field of 0.4 T. After cooled to 2 K under zero magnetic field, data were collected on warming at a rate of 3 K/min. FC-C and FC-W data collection used the same rate of 3 K/min.

8. DFT calculations

The first-principles calculations were performed with the density functional theory using the projector augmented wave method [39] implemented in the Vienna *Ab Initio* simulation package [40,41]. The exchange-correlation potential is described by generalized gradient approximation (GGA) of Perdew-Burke-Ernzerhof functions [42]. Strong electron-electron correlation beyond GGA for nickel 3*d* electrons is supplemented by plus Hubbard *U* (GGA+*U*) calculations with Dudarev's approach [43], and we choose *U* = 4 eV in this work. An energy cutoff of 600 eV for the plane-wave expansion and a $7 \times 6 \times 1$ Monkhorst-Pack grid for *k*-point sampling are adopted for self-consistent calculations with good convergence (with accuracy at 10^{-6} eV). The crystal structure was fixed to the experimentally refined lattice constants obtained from single crystal x-ray diffraction (SXRD).

-
- [1] B. Keimer, S. A. Kivelson, M. R. Norman, S. Uchida, and J. Zaanen, From quantum matter to high-temperature superconductivity in copper oxides, *Nature (London)* **518**, 179 (2015).
- [2] C. Park and R. L. Snyder, Perovskite stacking in the structures of the high temperature cuprate superconductors, *Appl. Supercond.* **3**, 73 (1995).
- [3] M. B. Salamon and M. Jaime, The physics of manganites: Structure and transport, *Rev. Mod. Phys.* **73**, 583 (2001).
- [4] M. Imada, A. Fujimori, and Y. Tokura, Metal-insulator transitions, *Rev. Mod. Phys.* **70**, 1039 (1998).
- [5] Y. S. Oh, X. Luo, F.-T. Huang, Y. Wang, and S.-W. Cheong, Experimental demonstration of hybrid improper ferroelectricity and the presence of abundant charged walls in $(\text{Ca}, \text{Sr})_3\text{Ti}_2\text{O}_7$ crystals, *Nat. Mater.* **14**, 407 (2015).
- [6] C. Lu, M. Wu, L. Lin, and J.-M. Liu, Single-phase multiferroics: New materials, phenomena, and physics, *Natl. Sci. Rev.* **6**, 653 (2019).
- [7] J. Zhang and X. Tao, Review on quasi-2D square planar nickelates, *CrystEngComm* **23**, 3249 (2021).
- [8] M. Hücker, K. Chung, M. Chand, T. Vogt, J. M. Tranquada, and D. J. Buttrey, Oxygen and strontium codoping of La_2NiO_4 : Room-temperature phase diagrams, *Phys. Rev. B* **70**, 064105 (2004).
- [9] H. L. Sun, M. W. Huo, X. W. Hu, J. Y. Li, Z. J. Liu, Y. F. Han, L. Y. Tang, Z. Q. Mao, P. T. Yang, B. S. Wang, J. G. Cheng, D. X. Yao, G. M. Zhang, and M. Wang, Signatures of superconductivity near 80 K in a nickelate under high pressure, *Nature (London)* **621**, 493 (2023).
- [10] Y. Zhang, D. Su, Y. Huang, H. Sun, M. Huo, Z. Shan, K. Ye, Z. Yang, R. Li, M. Smidman, M. Wang, L. Jiao, and H. Yuan, High-temperature superconductivity with zero-resistance and strange metal behavior in $\text{La}_3\text{Ni}_2\text{O}_7$, [arXiv:2307.14819](https://arxiv.org/abs/2307.14819).
- [11] Y. Zhou, J. Guo, S. Cai, H. Sun, P. Wang, J. Zhao, J. Han, X. Chen, Qi Wu, Y. Ding, M. Wang, T. Xiang, H.-k. Mao, and L. Sun, Evidence of filamentary superconductivity in pressurized $\text{La}_3\text{Ni}_2\text{O}_7$ single crystals, [arXiv:2311.12361](https://arxiv.org/abs/2311.12361).
- [12] J. Hou, P.-T. Yang, Z.-Y. Liu, J.-Y. Li, P.-F. Shan, L. Ma, G. Wang, N.-N. Wang, H.-Z. Guo, J.-P. Sun, Y. Uwatoko, M. Wang, G.-M. Zhang, B.-S. Wang, and J.-G. Cheng, Emergence of high-temperature superconducting phase in pressurized $\text{La}_3\text{Ni}_2\text{O}_7$ crystals, *Chin. Phys. Lett.* **40**, 117302 (2023).
- [13] J. Zhang, A. S. Botana, J. W. Freeland, D. Phelan, H. Zheng, V. Pardo, M. R. Norman, and J. F. Mitchell, Large orbital polarization in a metallic square-planar nickelate, *Nat. Phys.* **13**, 864 (2017).

- [14] Y. M. Klein, M. Kozłowski, A. Linden, P. Lacorre, M. Medarde, and D. J. Gawryluk, RENiO₃ single crystals (RE = Nd, Sm, Gd, Dy, Y, Ho, Er, Lu) grown from molten salts under 2000 bar of oxygen gas pressure, *Cryst. Growth Des.* **21**, 4230 (2021).
- [15] F. Li, S. Wang, C. Ma, X. Wang, C. Liu, C. Fan, L. Han, S. Wang, X. Tao, and J. Zhang, Flux growth of trilayer La₄Ni₃O₁₀ single crystals at ambient pressure, *Cryst. Growth Des.* **24**, 347 (2024).
- [16] See Supplemental Material at <http://link.aps.org/supplemental/10.1103/PhysRevMaterials.8.053401> for more details of single crystals, unit cell determination, single-crystal x-ray diffraction data refinement, STEM, and DFT+U results of La₂NiO₄ · La₃Ni₂O₇.
- [17] M. Zhang, C. Pei, Q. Wang, Y. Zhao, C. Li, W. Cao, S. Zhu, J. Wu, and Y. Qi, Effects of pressure and doping on Ruddlesden-Popper phases La_{n+1}Ni_nO_{3n+1}, *J. Mater. Sci. Technol.* **185**, 147 (2024).
- [18] G. Wang, N. Wang, Y. Wang, L. Shi, X. Shen, J. Hou, H. Ma, P. Yang, Z. Liu, H. Zhang, X. Dong, J. Sun, B. Wang, K. Jiang, J. Hu, Y. Uwatoko, and J. Cheng, Observation of high-temperature superconductivity in the high-pressure tetragonal phase of La₂PrNi₂O_{7-δ}, [arXiv:2311.08212](https://arxiv.org/abs/2311.08212).
- [19] Z. Liu, H. Sun, M. Huo, X. Ma, Y. Ji, E. Yi, L. Li, H. Liu, J. Yu, Z. Zhang, Z. Chen, F. Liang, H. Dong, H. Guo, D. Zhong, B. Shen, S. Li, and M. Wang, Evidence for charge and spin density waves in single crystals of La₃Ni₂O₇ and La₃Ni₂O₆, *Sci. China: Phys. Mech. Astron.* **66**, 217411 (2023).
- [20] J. Zhang, H. Zheng, Y.-S. Chen, Y. Ren, M. Yonemura, A. Huq, and J. F. Mitchell, High oxygen pressure floating zone growth and crystal structure of the metallic nickelates R₄Ni₃O₁₀ (R = La, Pr), *Phys. Rev. Mater.* **4**, 083402 (2020).
- [21] J. Zhang, D. Phelan, A. S. Botana, Y.-S. Chen, H. Zheng, M. Krogstad, S. G. Wang, Y. Qiu, J. A. Rodriguez-Rivera, R. Osborn, S. Rosenkranz, M. R. Norman, and J. F. Mitchell, Intertwined density waves in a metallic nickelate, *Nat. Commun.* **11**, 6003 (2020).
- [22] S. Catalano, M. Gibert, J. Fowlie, J. Íñiguez, J. M. Triscone, and J. Kreisel, Rare-earth nickelates RNiO₃: Thin films and heterostructures, *Rep. Prog. Phys.* **81**, 046501 (2018).
- [23] M. Greenblatt, Ruddlesden-Popper Ln_{n+1}Ni_nO_{3n+1} nickelates: Structure and properties, *Curr. Opin. Solid State Mater. Sci.* **2**, 174 (1997).
- [24] G. A. Pan, Q. Song, D. Ferenc Segedin, M.-C. Jung, H. El-Sherif, E. E. Fleck, B. H. Goodge, S. Doyle, D. Córdoba Carrizales, A. T. N'Diaye, P. Shafer, H. Paik, L. F. Kourkoutis, I. El Baggari, A. S. Botana, C. M. Brooks, and J. A. Mundy, Synthesis and electronic properties of Nd_{n+1}Ni_nO_{3n+1} Ruddlesden-Popper nickelate thin films, *Phys. Rev. Mater.* **6**, 055003 (2022).
- [25] J. Song, X. Jin, S. Zhang, X. Jiang, J. Yang, Z. Li, J. Zhou, H. Zhang, and Y. Nie, Synergistic role of E_g filling and anion-cation hybridization in enhancing the oxygen evolution reaction activity in nickelates, *ACS Appl. Energy Mater.* **4**, 12535 (2021).
- [26] B. Raveau and M. M. Seikh, *Cobalt Oxides: From Crystal Chemistry to Physics* (Wiley-VCH Verlag & Co. KGaA, Weinheim, 2012).
- [27] Y. Chen, Y. Sun, J. Peng, J. Tang, K. Zheng, and Z. Liang, 2D Ruddlesden-Popper perovskites for optoelectronics, *Adv. Mater.* **30**, 1703487 (2018).
- [28] M. Han, Y. Xiao, C. Zhou, Y. Yang, X. Wu, Q. Hu, X. Jin, W. Zhang, J.-S. Hu, and Y. Jiang, Recent advances on two-dimensional metal halide perovskite x-ray detectors, *Mater. Futures* **2**, 012104 (2023).
- [29] F. Liu, R. Wu, J. Wei, W. Nie, A. D. Mohite, S. Brovelli, L. Manna, and H. Li, Recent progress in halide perovskite radiation detectors for gamma-ray spectroscopy, *ACS Energy Lett.* **7**, 1066 (2022).
- [30] H. Kim, J. Bertinshaw, J. Porras, B. Keimer, J. Kim, J. W. Kim, J. Kim, J. Kim, G. Noh, G. Y. Kim, S. Y. Choi, and B. J. Kim, Sr₂IrO₄/Sr₃Ir₂O₇ superlattice for a model two-dimensional quantum Heisenberg antiferromagnet, *Phys. Rev. Res.* **4**, 013229 (2022).
- [31] P. Lacorre, Passage from T-type to T'-type arrangement by reducing R₄Ni₃O₁₀ to R₄Ni₃O₈ (R = La, Pr, Nd), *J. Solid State Chem.* **97**, 495 (1992).
- [32] V. V. Poltavets, K. A. Lokshin, S. Dikmen, M. Croft, T. Egami, and M. Greenblatt, La₃Ni₂O₆: A new double T'-type nickelate with infinite Ni^{1+/2+}O₂ layers, *J. Am. Chem. Soc.* **128**, 9050 (2006).
- [33] D. Li, K. Lee, B. Y. Wang, M. Osada, S. Crossley, H. R. Lee, Y. Cui, Y. Hikita, and H. Y. Hwang, Superconductivity in an infinite-layer nickelate, *Nature (London)* **572**, 624 (2019).
- [34] X. Chen, J. Zhang, A. S. Thind, S. Sharma, H. LaBollita, G. Peterson, H. Zheng, D. P. Phelan, A. S. Botana, R. F. Klie, and J. F. Mitchell, Polymorphism in the Ruddlesden-Popper nickelate La₃Ni₂O₇: Discovery of a hidden phase with distinctive layer stacking, *J. Am. Chem. Soc.* **146**, 3640 (2024).
- [35] P. Puphal, P. Reiss, N. Enderlein, Y.-M. Wu, G. Khaliullin, V. Sundaramurthy, T. Priessnitz, M. Knauff, L. Richter, M. Isobe, P. A. van Aken, H. Takagi, B. Keimer, Y. Eren Suyolcu, B. Wehinger, P. Hansmann, and M. Hepting, Unconventional crystal structure of the high-pressure superconductor La₃Ni₂O₇, [arXiv:2312.07341](https://arxiv.org/abs/2312.07341).
- [36] H. Wang, L. Chen, A. Rutherford, H. Zhou, and W. Xie, Long-range structural order in a hidden phase of Ruddlesden-Popper bilayer nickelates La₃Ni₂O₇, *Inorg. Chem.* **63**, 5020 (2024).
- [37] Bruker. Computer code APEX4; Bruker Analytical x-ray instruments, Inc.: Madison, Wisconsin, USA, 2022.
- [38] O. V. Dolomanov, L. J. Bourhis, R. J. Gildea, J. A. K. Howard, and H. Puschmann, OLEX2: A complete structure solution, refinement and analysis program, *J. Appl. Crystallogr.* **42**, 339 (2009).
- [39] P. E. Blöchl, Projector augmented-wave method, *Phys. Rev. B* **50**, 17953 (1994).
- [40] G. Kresse and J. Furthmüller, Efficient iterative schemes for *ab initio* total-energy calculations using a plane-wave basis set, *Phys. Rev. B* **54**, 11169 (1996).
- [41] G. Kresse and D. Joubert, From ultrasoft pseudopotentials to the projector augmented-wave method, *Phys. Rev. B* **59**, 1758 (1999).
- [42] J. P. Perdew, K. Burke, and M. Ernzerhof, Generalized gradient approximation made simple, *Phys. Rev. Lett.* **77**, 3865 (1996).
- [43] S. L. Dudarev, G. A. Botton, S. Y. Savrasov, C. J. Humphreys, and A. P. Sutton, Electron-energy-loss spectra and the structural stability of nickel oxide: An LSDA+U study, *Phys. Rev. B* **57**, 1505 (1998).